Monthly Notices
of the
ROYAL ASTRONOMICAL SOCIETY

MNRAS **482,** 980–987 (2019)
Advance Access publication 2018 October 12

doi:10.1093/mnras/sty2761

A likely runaway star cluster in the outer disc of the Large Magellanic Cloud

Andrés E. Piatti,[1,2]★ Ricardo Salinas [3] and Eva K. Grebel[4]

[1]*Consejo Nacional de Investigaciones Científicas y Técnicas, Av. Rivadavia 1917, C1033AAJ Buenos Aires, Argentina*
[2]*Observatorio Astronómico, Universidad Nacional de Córdoba, Laprida 854, X5000BGQ Córdoba, Argentina*
[3]*Gemini Observatory, Casilla 603, La Serena, Chile*
[4]*Astronomisches Rechen-Institut, Zentrum für Astronomie der Universität Heidelberg, Mönchhofstr. 12-14, D-69120 Heidelberg, Germany*

Accepted 2018 October 9. Received 2018 October 3; in original form 2018 June 17

ABSTRACT

We present results from photometric and spectroscopic data obtained with SOAR and Gemini observatory facilities in the field of a recently discovered star cluster. The cluster, projected towards the Eastern side of the outer disc of the Large Magellanic Cloud (LMC), was originally placed nearly 10 kpc behind the LMC with an age and metallicity typical of the innermost LMC star cluster population. We assigned radial velocity (RV) memberships to stars observed spectroscopically, and derived the cluster age and distance from theoretical isochrone fitting to the cluster colour–magnitude diagram. The new object turned out to be a 0.9 Gyr old outer LMC disc cluster, which possibly reached the present position after being scattered from the innermost LMC regions where it might have been born. We arrived at this conclusion by examining the spatial distribution of LMC star clusters of similar age, by comparing the derived spectroscopic metallicity with that expected for an outside-in galaxy formation scenario, by considering the cluster internal dynamical stage as inferred from its derived structural parameters and by estimating the circular velocity of a disc that rotates with the corresponding star cluster radial velocity at the cluster's deprojected distance, which resulted to be nearly 60 per cent higher than that of most of the outer LMC disc clusters.

Key words: galaxies: individual: LMC – galaxies: star clusters: general.

1 INTRODUCTION

Recently, Piatti (2016) discovered a star cluster towards the Eastern part of the Large Magellanic Cloud (LMC) outer disc that appeared to be located behind the LMC at the Small Magellanic Cloud (SMC)'s distance. He speculated about the possibility of it being the first discovered cluster that was born in the LMC and soon ejected into the intergalactic space during the recent Milky Way/Magellanic Clouds (MW/MCs) interaction (Kallivayalil et al. 2013; Casetti-Dinescu et al. 2014; Indu & Subramaniam 2015).

The cluster deserves more of our attention in order to unveil its actual origin, particularly in the light of the implications that such an unusual object could have for our understanding of the cluster formation in the LMC. LMC outer disc clusters have long been commonly thought to be old and hence, to be key to reconstructing the early galaxy formation and chemical enrichment history (Piatti et al. 2009; Glatt, Grebel & Koch 2010). However, the recently discovered cluster does not comply with such a picture, because it seems to be younger (age $\sim$ 280 Myr, Piatti 2016) than what should be expected. Likewise, the outer disc is commonly featured as a more metal-poor structure ([Fe/H] $\lesssim -0.5$ dex) than the inner LMC body (Harris & Zaritsky 2009; Meschin et al. 2014), although the new cluster ([Fe/H] $\sim-$ 0.1 dex, Piatti 2016) is at the metal-rich end of the LMC cluster metallicity distribution, making it a really odd object.

A network of streams surrounding the LMC has been discovered (see e.g. Belokurov & Koposov 2016; Mackey et al. 2016) that could be relics of collisions between both MCs (Hammer et al. 2015; Salem et al. 2015) and possibly the MW. However, no cluster has been discovered so far in those streams (e.g. Moni Bidin et al. 2017), except for those in the Magellanic Bridge (e.g. Bica et al. 2015; Piatti et al. 2015), which is located on the opposite side of the LMC with respect to the newly discovered cluster. Moreover, the new cluster is located towards a direction where no stream has been seen yet. Although the spatial distribution of the latest discovered clusters demonstrates that the outer regions of the MCs were less explored in the past (see e.g. Pieres et al. 2016; Sitek et al. 2016; Piatti 2017), the aforementioned newly discovered cluster is positioned at an LMC-centric distance where no clusters are expected to have formed.

To unveil the origin of this potentially very unusual cluster, we have conducted a photometric and spectrocopic study from which we comprehensively derive its astrophysical properties. The obser-

★ E-mail: andres@oac.unc.edu.ar

© 2018 The Author(s)
Published by Oxford University Press on behalf of the Royal Astronomical Society

Downloaded from https://academic.oup.com/mnras/article/482/1/980/5128516 by guest on 01 February 2021

Table 1. *gi* data of stars in the field of the new star cluster[a].

Star	RA (deg)	DEC. (deg)	g (mag)	$\sigma(g)$ (mag)	i (mag)	$\sigma(i)$ (mag)	$\chi(g)$	sharp(g)	$\chi(i)$	sharp(i)
–	–	–	–	–	–	–	–	–	–	–
626	90.89030115	−72.42108798	23.510	0.087	23.046	0.055	1.006	−0.304	1.079	0.400
627	90.88438994	−72.42100738	22.000	0.022	21.521	0.015	0.986	0.062	1.061	−0.194
628	90.94368341	−72.42106770	22.168	0.026	21.364	0.013	1.015	0.225	1.013	0.165
–	–	–	–	–	–	–	–	–	–	–

Note. [a]A portion of the table is presented here for guidance of its contents. The entire table is available as Supplementary material in the online version of the journal.

vations are described in Section 2, while radial velocity (RV) and metallicity membership probabilities are presented in Section 3. In Section 4, we estimate the cluster's astrophysical properties and discuss their implications for the cluster origin. We found that the cluster is not as extreme as originally estimated by Piatti (2016). Finally, the main conclusions of this work are summarized in Section 5.

2 OBSERVATIONAL DATA

2.1 SOAR/SAMI observations

The cluster was observed on 2018 January 3 with the SOAR Adaptive Module (SAM) coupled with its Imager (SAMI), installed at the SOAR 4.1m telescope at Cerro Pachón, Chile. SAM is a ground-layer adaptive optics system correcting atmospheric turbulence near the ground. Technical details of the instrument can be found in Tokovinin et al. (2016). SAMI provides a field of view (FOV) of 3×3 arcmin^2 with a pixel scale of 0.091 arcsec when used with a 2×2 binning. Observations were taken in the SDSS g and i filters, with 3×300 and 3×200 s exposures, at mean-corrected full width at half-maximums of the stellar images of 0.54 arcsec in g and 0.41 arcsec in i, respectively.

2.1.1 *Data reduction and photometry*

SAMI images were reduced employing the multi-instrument imaging pipeline THELI[1] (Schirmer 2013), by applying bias subtraction and flat-fielding the images with bias and twilight sky frames taken during the same night. After flat-fielding, a difference of a few per cent was still visible in the background between the four SAMI amplifiers. This was removed applying a collapse correction implemented within THELI.

The images were not combined. Instead the photometry was done in each of them separately with the DAOPHOT/ALLSTAR suite of programs (Stetson 1987). The procedure involved the following steps: (a) adding back to each image a mean sky background level that had been subtracted during the collapse correction. This is necessary for DAOPHOT to have the proper photon statistics. (b) Sources in each field were searched with SExtractor (Bertin & Arnouts 1996) combining a Gaussian filter and a 'Mexican hat' filter; an approach that enhances the detection of both faint sources and sources near very bright ones (e.g. Salinas et al. 2015). (c) Nearly 40 bright and reasonably isolated point sources were selected in the image with the best image quality, in order to model the point spread function (PSF) as a quadratically varying Moffat function as performed in previous studies with the same instrument (Fraga, Kunder & Tokovinin 2013; Salinas et al. 2016). The resulting PSF-subtracted images revealed no significant increase of the residuals as function of radius across the whole small FOV (3×3 arcmin^2). Finally, the PSF photometry was obtained using the ALLSTAR task (Stetson 1987), and all measurements per filter were averaged using DAOMASTER's routines (Stetson 1992). Aperture corrections were calculated based on a subset of PSF stars and instrumental magnitudes converted into standard ones using transformation equations derived from observations of standard star fields observed during the same night. The transformation equations were fitted with rms of 0.011 mag and 0.012 mag for g and i, respectively, as given by IRAF/PHOTCAL. Table 1 shows a portion of the resulting photometric data set, while Fig. 1 depicts the colour–magnitude diagram (CMD) built from all the measured stars.

[1]https://www.astro.uni-bonn.de/theli/gui/background.html

2.1.2 *Photometric completeness*

The photometric completeness was derived from standard artificial star experiments on all observed images using the DAOPHOT.ADDSTAR task. To do this, we added 300 stars with i magnitudes between 16 and 25 mag, following an exponential distribution in order to achieve a better statistics at the fainter limit. Two-thirds of the stars were randomly distributed within the SAMI FOV, while the remaining one-third was distributed following a two-dimensional Gaussian distribution centred on the cluster. The initial g magnitudes for the ADDSTAR experiments were calculated from the i magnitudes using a polynomial fit to the main features in the CMD. The experiment was repeated 30 times per observed image for a total of 9000 artificial stars. All frames with the added stars were photometered exactly as the original frames. Input and output catalogues were matched using a combination of DAOMASTER (Stetson 1992) and STILTS (Taylor 2006).

Fig. 1 shows the results of the completeness experiments for a radial bin with $R < 10$ arcsec and $R > 60$ arcsec. Differences in radial completeness are almost negligible and a very small difference is seen between the filters. Additionally, the results were fitted with a 'Pritchett function' (McLaughlin, Harris & Hanes 1994), commonly used in globular cluster systems studies (e.g. Salinas et al. 2015), which can be seen as dotted and dash–dotted lines, respectively.

2.2 GMOS-S/MOS observations

Spectroscopic observations were obtained with the Gemini Multi-Object Spectrograph (GMOS, Hook et al. 2004), mounted on the 8.1m Gemini South telescope, located on Cerro Pachón, Chile, on the nights of 2018 April 20 and 2018 April 21. GMOS is equipped with three Hamamatsu CCDs (Gimeno et al. 2016) yielding a total FOV of 5.5 × 5.5 arcmin^2. Given the very compact nature of the new star cluster, two masks were designed, including five and three

Downloaded from https://academic.oup.com/mnras/article/482/1/980/5128516 by guest on 01 February 2021

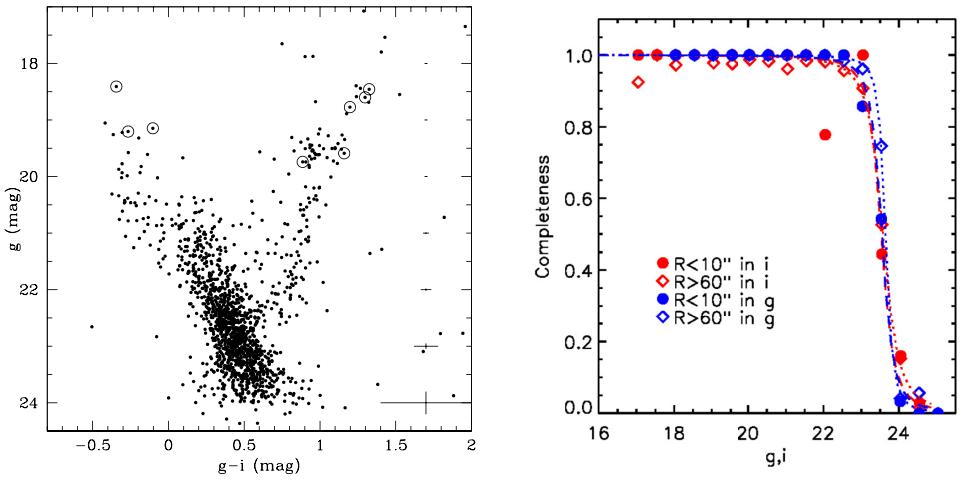

Figure 1. Observed CMD of stars in the field of the new star cluster (left-hand panel) and the completeness curves obtained from our photometry (right). Photometry errors are represented by error bars at the CMD's right margin, and spectroscopic targets are encircled.

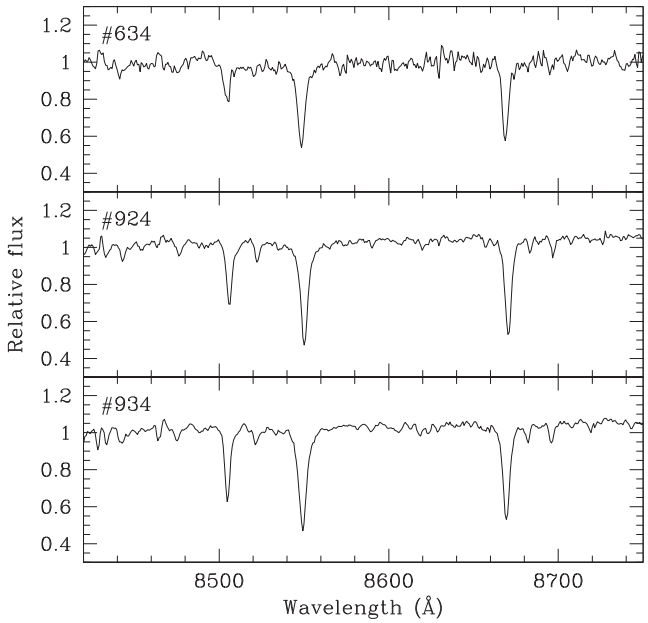

Figure 2. Normalized spectra of some observed stars. Star numbers are as in Table 2.

stars, respectively, selected from Piatti (2016, see some examples in Fig. 2). Observations were taken with the R831 grating, centred at 850 nm, providing a resolving power of $R \sim 2200$ for 1 arcsec slitlets. Exposures of 3 × 900 s were obtained for each mask.

Data reduction was done with standard techniques implemented within the Gemini IRAF[2] package. After bias subtraction, flat-fielding and wavelength calibration with CuAr spectra taken right after the science observations, the zero-point of the latter was corrected by measuring the position of bright, isolated skylines near the CaT region identified from a UVES high-resolution spectrum (Hanuschik 2003). The shifts in the zero-point were found to be no larger than 0.5 Å. After this correction, spectra were sky-subtracted, extracted, and combined following standard methods. Fig. 2 illustrates some of the obtained spectra.

[2]IRAF is distributed by the National Optical Astronomy Observatories, which is operated by the Association of Universities for Research in Astronomy, Inc., under contract with the National Science Foundation.

3 RADIAL VELOCITY AND METALLICITY MEASUREMENTS

RVs were measured with the cross-correlation algorithm of Tonry & Davis (1979) as implemented in IRAF FXCOR task. 40 spectra were selected from the library of Cenarro et al. (2001) from a list of 706 stars observed in the 8348−9020 Å region with a resolution of 1.5 Å. This template subsample included stars with late O to late M spectral types. Each science spectrum was then cross-correlated against the whole template subsample, and the five measurements with the highest cross-correlation peak were averaged to obtain a final RV per star, which include heliocentric corrections. Table 2 shows the measured signal-to-noise (S/N) ratio in the region of the CaII triplet lines and the resulting RVs with their uncertainties.

The RV distribution function was then constructed by summing all the individual RV values. We represented each RV value by a Gaussian function with centre and full width at half maximum equal to the mean RV value and 2.355 times the associated error, respectively (see Table 2), and assigned to each Gaussian the same amplitude. Fig. 3 shows the resulting RV distribution function, where the shaded region represents the cluster RV range adopted on the basis of the largest number of stars with similar RV measurements. Hence, the mean cluster RV computed from stars #634, 748, and 836 turned out to be 215.3 ± 3.1 km s^{-1}.

We then measured equivalent widths of the CaII infrared triplet lines of the observed red giants using the SPLOT package within IRAF. Their resulting values and uncertainties are listed in Table 2. The latter were estimated by considering upper and lower envelopes of the continuum at both sides of the CaII lines. Piatti et al. (2018) showed that this procedure of measuring CaII lines equivalent widths is highly consistent with no systematic offset with respect to the techniques employed by Cole et al. (2004, 2005) and Da Costa (2016), among others. Then we overplotted the sum of the equivalent widths of the three CaII lines (ΣW(CaII)) in the ΣW(CaII) versus $V - V_{RC}$ plane, which has been calibrated in terms of metallicity (see e.g. Cole et al. 2004, 2005). In that dia-

Downloaded from https://academic.oup.com/mnras/article/482/1/980/5128516 by guest on 01 February 2021

Table 2. Radial velocities, CaII triplet line equivalent widths, and metallicities of selected stars. Spectra with S/N = 15 were only useful to measure RVs.

Star[a]	S/N	RV	W8498	W8542	W8662	[Fe/H]
634	32	216.9 ± 2.0	1.131 ± 0.012	3.552 ± 0.128	2.177 ± 0.029	−0.48 ± 0.20
724	45	275.9 ± 2.1	1.208 ± 0.053	3.504 ± 0.118	2.221 ± 0.106	−0.52 ± 0.23
748	60	218.0 ± 2.0	1.450 ± 0.050	3.623 ± 0.045	2.776 ± 0.031	−0.46 ± 0.17
796	15	259.4 ± 6.6	–	–	–	–
836	15	211.0 ± 7.0	–	–	–	–
868	15	305.0 ± 11.0	–	–	–	–
924	65	275.3 ± 2.0	1.838 ± 0.095	3.907 ± 0.033	2.736 ± 0.040	−0.18 ± 0.19
934	60	238.8 ± 2.0	1.909 ± 0.134	3.801 ± 0.059	2.692 ± 0.040	−0.30 ± 0.21

Note. [a] Star numbers are as in Table 1.

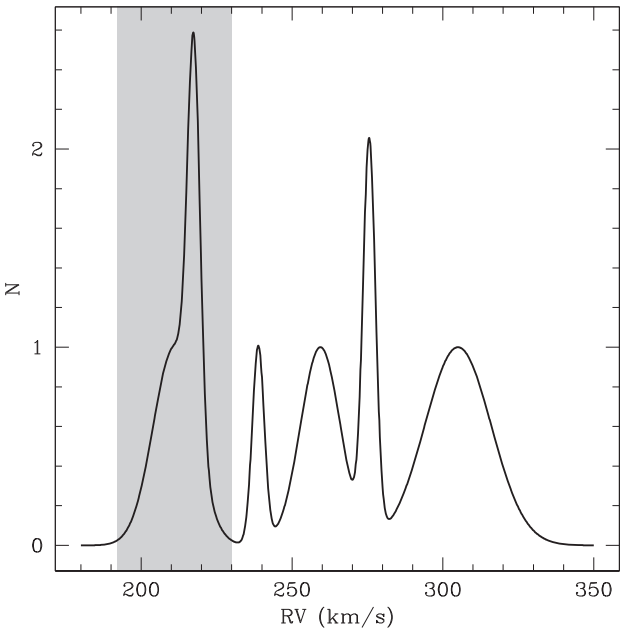

Figure 3. RV distribution function for stars observed in the field of the new star cluster. The shaded region represents the adopted cluster RV range.

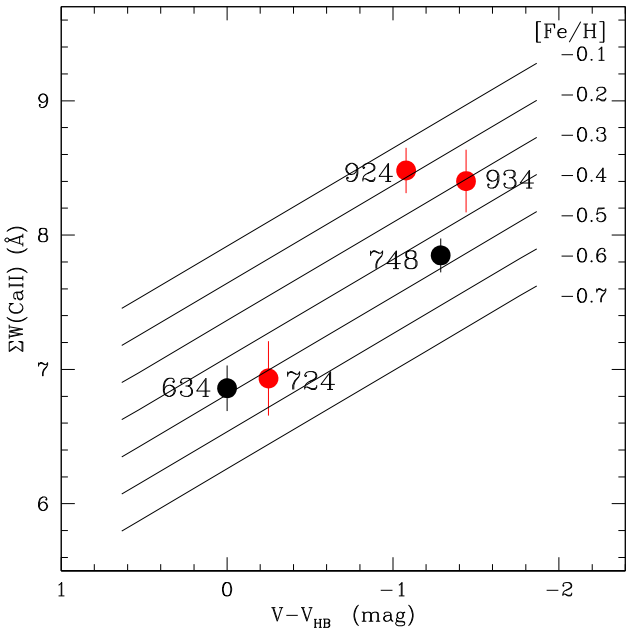

Figure 4. Sum of the CaII triplet line equivalent widths as a function of $V - V_{\rm HB}$ for stars observed in the field of the new star cluster. The star numbers according to Table 2 and the error bars are included. The black and red filled cirles represent probable cluster member and non-member stars, respectively (see text for details). Iso-abundance lines derived by Cole et al. (2004) for some [Fe/H] values are also depicted.

gram $V_{\rm RC}$ refers to the mean magnitude of the cluster red clump. In this case, we first converted g magnitudes into Johnson V ones using the expression:

$$V = g - 0.3557 * (g - i) - 0.0600, \quad (1)$$

which we obtained from Lupton's (2005)[3] transformation equations between *ugriz* and $UBVR_{\rm c}I_{\rm c}$ photometric systems and the relationship $g - i = (g - r) + (r - i)$. We adopted for the new star cluster $g_{\rm RC} = 19.74$ mag (see Fig. 6). Fig. 4 shows the resulting ΣW(CaII) versus $V - V_{\rm RC}$ diagram, where we included iso-abundance lines according to equation (5) of Cole et al. (2004) for $\beta = 0.73$ Å mag^{-1}, while the interpolated [Fe/H] values are listed in the last column of Table 2. Note that the influence of age on equation (5) is relatively small, so that it can be applied to stellar systems with ages as young as ∼ 0.3 Gyr

(see Cole et al. 2004; Carrera et al. 2007; Da Costa 2016). We calculated the [Fe/H] errors by propagating those of the coefficients in equation (5) and $\sigma(\beta)$ (Cole et al. 2004), the photometric errors (Table 1), and σ(ΣW(CaII)) (Table 2), respectively. As can be seen, the likely red giant RV members (stars #634 and 748) also share a very similar metallicity of ∼ −0.5 dex. The remaining red giants have interpolated [Fe/H] values falling well within the LMC field star metallicity range (Cole et al. 2005; Piatti & Geisler 2013), but cover a metallicity range too wide to be consistent with cluster membership, further strenghtening our conclusions regarding the cluster parameters.

4 ANALYSIS AND DISCUSSION

The mean star cluster metallicity helped us to select the appropriate theoretical isochrone to match the cluster CMD. In doing that, we used the well-established colour excess $E(B - V) = 0.08 \pm 0.01$ mag, also confirmed from the NASA/IPAC Extragalactic Data base[4]

[3] http://www.sdss.org/dr13/algorithms/sdssUBVRITransform/#Lupton2005.

[4] http://ned.ipac.caltech.edu/. NED is operated by the Jet Propulsion Laboratory, California Institute of Technology, under contract with NASA.

Downloaded from https://academic.oup.com/mnras/article/482/1/980/5128516 by guest on 01 February 2021

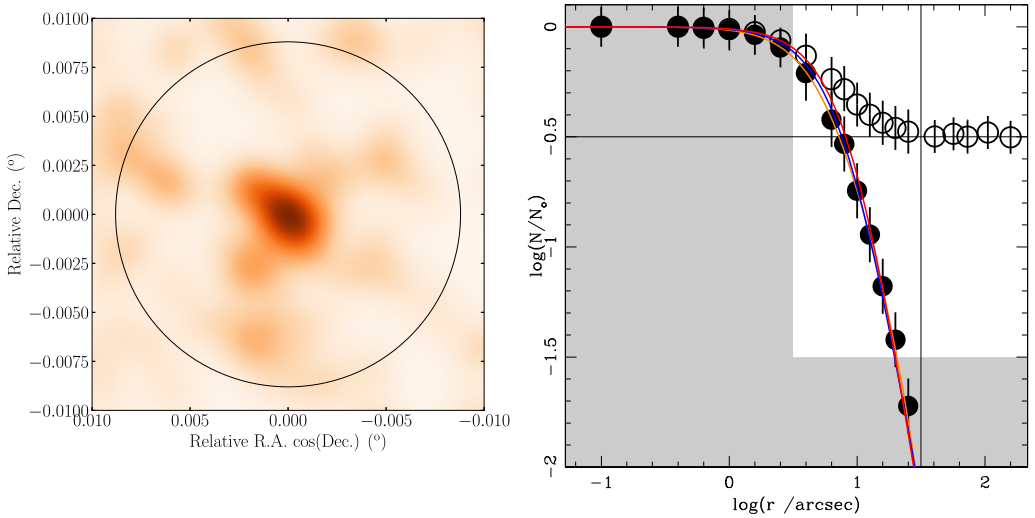

Figure 5. *Left:* Stellar density map centred on the new star cluster, smoothed by a Gaussian kernel with standard deviation 3.6 arcsec. The black circle represents the cluster radius. *Right :* Normalized observed and background-subtracted cluster stellar radial profiles depicted with open and filled circles, respectively. The error bars are also included. The horizontal and vertical lines represent the mean background level and the adopted cluster radius, respectively. The best-fitting King (1962), Elson et al. (1987), and Plummer (1911) models are superimposed with solid orange, blue, and red lines, respectively. The shaded area represents the region not considered by Piatti (2016).

(NED), as well as one upper main sequence (MS) and the two red giant RV members to better constrain the cluster age and distance.

With the aim of reproducing the cluster CMD, we first built the cluster stellar radial profile from which we derived its radius, namely: the intersection of the cluster density profile with the mean background level. For distances smaller than 10 arcsec from the cluster centre, the cluster radial profile was built by averaging the generated values in the stellar density map constructed from a kernel density estimator (KDE) technique. As can be seen in Fig. 5, the stellar density map resulted in a nearly smoothly continuing distribution of density values that allowed us to trace more accurately the cluster radial profile in the innermost regions, instead of using small boxes to count stars inside them. Star counts within appropriate size boxes were more suitable to delineate the outer regions of the cluster profile as well as the background level, because of the lack of spurious fluctuations due to the small number statistics.

We run both the KDE routine and the counting of stars over a subsample of stars with g magnitudes brighter than those for the 90 per cent completeness level (see Fig. 1). The KDE was repeatedly run by employing a Gaussian function with bandwidths between 1.8 and 4.8 arcsec in steps of 0.6, while the star counts were performed using boxes with sizes between 4.0 and 8.0 arcsec in steps of 1.0 arcsec, respectively. The resulting averaged cluster radial profile is shown in Fig. 5 (open circles) with the respective error bars. The mean background level was then estimated by averaging those values for $\log(r/\mathrm{arcsec}) \geq 1.7$ (horizontal line in Fig. 5). We chose this limit because it is readily visible from the figure that a meaningful mean background can be obtained from the values beyond it. Hence, the intersection of cluster radial profile with that mean background level resulted to be at $\log(r/\mathrm{arcsec}) = 1.55 \pm 0.10$ ($31.6^{+8.0}_{-6.0}$ arcsec), in excellent agreement with the cluster radius estimated by Piatti (2016). Note that all the stars observed spectroscopically lie inside the cluster radius.

The background-subtracted cluster radial profile (filled circles in Fig. 5), with error bars that come from considering in quadrature the uncertainties of the measured profile and the dispersion of the background level, surpasses that previously traced by Piatti (2016), in the sense that it reaches the innermost regions of the cluster. This is mainly because the present cluster profile was built from a nearly continuous density map rather than from star counts. Likewise, we now reach fainter outermost cluster structures, despite the fact that we constrained the sample of stars to those with $g \lesssim 22.0$ mag, for completeness reasons. For the sake of the reader, we have shaded these regions in the figure. By using the present more extended cluster radial profile, we followed the procedure described in detail by Piatti & Mackey (2018) to fit King (1962), Elson, Fall & Freeman (1987), and Plummer (1911) models and thus to obtain accurate cluster structural parameters. We derived a cluster core radius (r_c) of 5.5 ± 0.5 arcsec, a half-light radius (r_h) of 12.0 ± 1.0 arcsec, a tidal radius (r_t) of 55.0 ± 5.0 arcsec, and a power-law index (γ, the slope at large radii in Fig. 5) of 3.5 ± 0.2, respectively.

Fig. 6 shows the extracted cluster CMD that results from using all the stars measured within the cluster radius. We have not carried out any star field decontamination so that, besides the cluster upper MS and red clump, the composite LMC star field MS at fainter magnitudes and few giant stars are also superimposed. We have drawn with bigger symbols stars for which we measured RVs, distinguishing those members from non-members with black filled circles and red boxes, respectively. At first glance, the three cluster members are fortunately placed in key positions as to perform a sound fitting of theoretical isochrones. To do that, we used as entries the known cluster reddening mentioned above and the spectroscopic metallicity derived in Section 3, allowing small variations according to their uncertainties; the only free parameters being the cluster age and distance modulus. As for the theoretical isochrones we used those computed by Bressan et al. (2012).

From a grid of values of age and distance modulus spread in the same ranges as in Piatti (2016), we found that the isochrone that best resembles the cluster features, namely: the upper MS, the MS turnoff from star #836, the base of the red clump from star #634, and the red giant branch from star #748, is that of $\log(t/\mathrm{yr}) = 8.95 \pm 0.05$ ($0.89^{+0.11}_{-0.10}$ Gyr) and $m - M_o = 18.40 \pm 0.05$ mag (d $= 47.9 \pm 1.1$ kpc), for a metallicity of [Fe/H] $= -0.4 \pm 0.1$ dex. The resulting cluster properties reveal that the object is not as

Downloaded from https://academic.oup.com/mnras/article/482/1/980/5128516 by guest on 01 February 2021

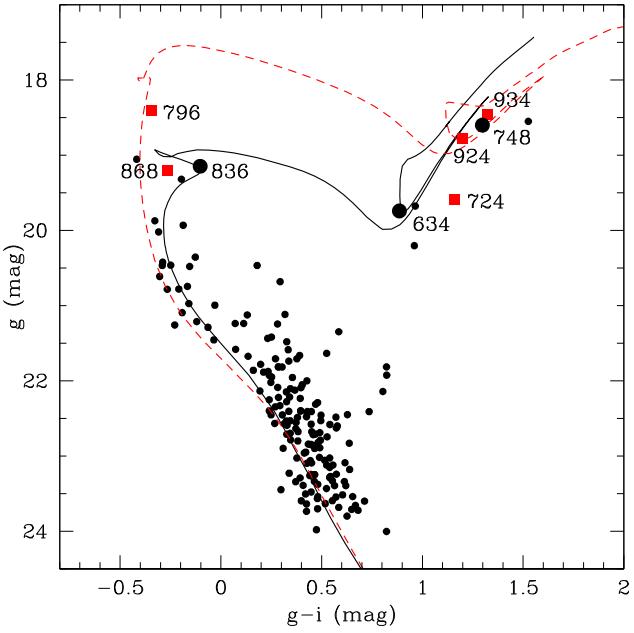

Figure 6. CMD of the observed stars located within the cluster radius. The red boxes and big black filled circles represent non-members and members according to their RVs and metallicities; their star numbers are also indicated (see Table 2). Theoretical isochrones of Bressan et al. (2012) for the present best solution ($\log(t/\mathrm{yr}) = 8.95$, [Fe/H] $= -0.4$ dex) and that of Piatti (2016) ($\log(t\ /\mathrm{yr}) = 8.45$, [Fe/H] $= -0.1$ dex) are superimposed with black solid and red dashed lines, respectively.

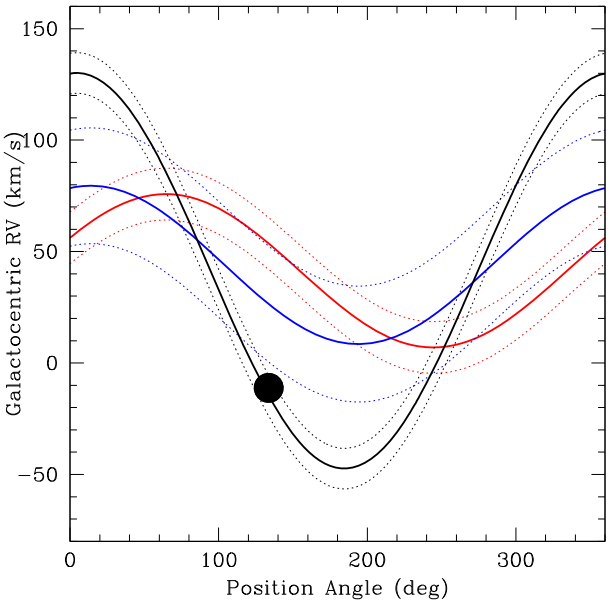

Figure 7. Position of the new star cluster in the Galactocentric RV versus PA diagram (filled circles). The error bars are smaller that the symbol size. The best solution for a disc that contains it is drawn with a black solid line, while the black dotted lines represent those considering every involved errors. We included the curves derived by Schommer et al. (1992, solution #3 in their table 3) from mostly outer LMC clusters and by van der Marel & Kallivayalil (2014) from *HST* proper motions of 22 LMC fields and 723 young field stars with blue and red solid lines, respectively, for comparison purposes. We include the derived errors in the rotational curves with dotted lines.

young, metal-rich or located as far away from the LMC as inferred by Piatti (2016), namely, age $= 0.28^{+0.04}_{-0.03}$ Gyr, [Fe/H]= -0.10 $\pm$ 0.05 dex, and d $= 60.3 \pm 1.4$ kpc, but one that lies in the main body of the galaxy with an age and a metal content that agree very well with the known picture of the LMC cluster age–metallicity relationship (Piatti & Geisler 2013). The inferred metallicity is in agreement with the [Fe/H] values and uncertainties of stars # 634 and 748 (see Table 2). Fig. 6 shows with a black solid line the best solution of the isochrone fitting, while the red dashed line represents the solution found by Piatti (2016). From the figure, it becomes clearer that the previous younger age, and hence larger distance and metallicity, come from considering a much brighter cluster MS turnoff and red clump. Here, the RV measurements allowed us to resolve the conundrum of its previously derived astrophysical properties.

We used the mean star cluster RV and its position angle (PA) to complementary assess the possible association of the cluster with the LMC disc (see Schommer et al. 1992; van der Marel et al. 2002; Grocholski et al. 2006; Sharma et al. 2010; van der Marel & Kallivayalil 2014). The cluster PA and its deprojected distance (ρ) were calculated considering a disc centred at RA= 80.05 $\pm$ 0.34° and Dec. $=-69.30 \pm 0.12°$, with an inclination $i = 26.2 \pm 5.9°$ and PA of the line-of-nodes $\Theta = 154.5 \pm 2.1°$, obtained by van der Marel & Kallivayalil (2014) from *HST* average proper motion measurements for stars in 22 fields and RVs of 723 young LMC field stars. We derived PA $= 131.4 \pm 3.0°$ and $\rho = 4.63 \pm 0.03°$, which implies that the new star cluster is located in the outer disc (Bica et al. 1998). We then converted the mean heliocentric cluster RV to the Galactocentric one through equation (4) in Feitzinger & Weiss (1979), in order to use the disc solutions found by Schommer et al. (1992). Fig. 7 shows the position of the new star cluster in the RV versus PA plane (filled circle) with the mean rotation curve obtained by Schommer et al. (1992, solution #3 in their table 3) using mostly outer LMC star clusters drawn with a blue solid line. In the figure, dotted blue lines represent the above solution with the uncertainties in the circular and systemic velocities and the derived dispersion velocity. The new star cluster appears to rotate in a slightly different disc than that containing most of the outer LMC star clusters. Likewise, it rotates even more differently than the young stellar population, as judged by the position and shape of the mean disc solution and those with its uncertainties and velocity dispersion found by van der Marel & Kallivayalil (2014) mentioned above, which we drew with red solid and dotted lines, respectively.

In order to characterize the disc that fully contains the new star cluster, we looked for the circular velocity ($v_{\rm rot}$) and PA of the line-of-nodes ($\mathrm{PA_{LOS}}$) of a disc that rotates at the deprojected cluster distance with the corresponding cluster RV. We evaluated equation (1) of Schommer et al. (1992) at the cluster PA for different values of ($v_{\rm rot}$, $\mathrm{PA_{LOS}}$) and then minimized by χ^2 the difference between the calculated and measured cluster RV. We used a grid of $v_{\rm rot}$ from 0.0 up to 200.0 km s^{-1} in steps of 1.0 km s^{-1}, and a range of $\mathrm{PA_{LOS}}$ from 0.0 up to 180.0 degrees in steps of 1.0 degree, besides the uncertainties in the cluster RV and PA. Thus, the most suitable disc turned out to be that with $v_{\rm rot} = 177.5 \pm 11.4$ km s^{-1} and $\mathrm{PA_{LOS}} = 94.5 \pm 2.7°$. This solution with its dispersion is drawn in Fig. 7 with black solid and dotted lines, respectively. When comparing our results with those for the outer LMC star clusters found by Schommer et al. (1992), i.e, $v_{\rm rot} = 71 \pm 8$ km s^{-1} and $\mathrm{PA_{LOS}} = 104 \pm 8°$, we found that the resulting disc is roughly oriented in the same direction, although it rotates with a circular velocity that is much higher.

We speculate that such a higher circular velocity is a consequence of having been scattered during an interaction with the

Downloaded from https://academic.oup.com/mnras/article/482/1/980/5128516 by guest on 01 February 2021

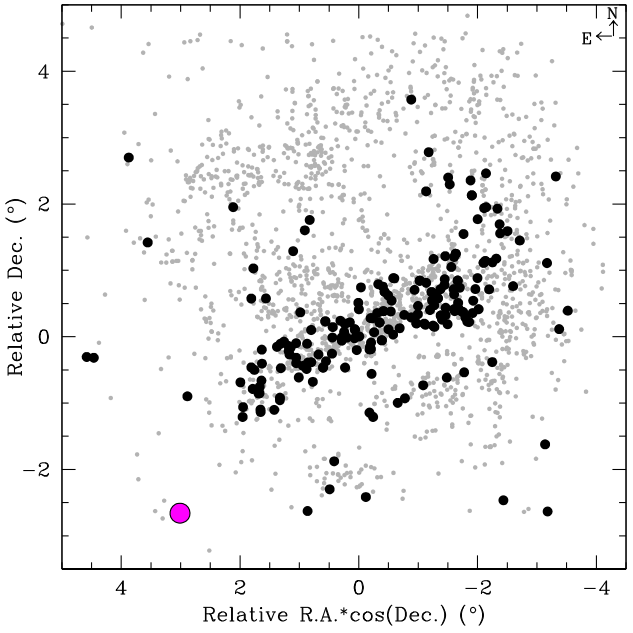

Figure 8. Spatial distribution of star clusters in Bica et al. (2008)'s catalogue and those with age estimates between log(*t*/yr) = 8.8 and 9.1 (Piatti 2014) drawn with grey and black circles, respectively. The new star cluster is represented by a magenta circle.

MW/SMC from the inner LMC regions (Kallivayalil et al. 2013; Casetti-Dinescu et al. 2014), where it may have formed. First, star clusters with age estimates within 3× σ (age) from the cluster age, i.e. log(*t*/yr) between 8.8 and 9.1 not only are statistically more concentrated in the LMC bar, but also very few star clusters have been identified in the outer Eastern side of the LMC disc. Therefore, it had to be scattered together with other star clusters of similar age towards an outer disc-like orbit. Fig. 8 illustrates the spatial distribution of star clusters in the Bica et al. (2008) catalogue with grey circles and those with ages between log(*t*/yr)= 8.8 and 9.1 – taken from the compilation of more than 2300 star clusters with age estimates (Piatti 2014) – drawn with black circles. The position in the sky of the new star cluster is represented by the magenta circle. Secondly, the metallicity level of field stars in the outer LMC disc ($\rho > 4^\circ$, <[Fe/H]> = -0.9 ± 0.2 dex) is on average more metal-poor than that for inner disc field stars ($\rho < 4^\circ$, <[Fe/H]> = -0.5 ± 0.2 dex) (see figure 3 in Piatti & Geisler 2013), in excellent agreement with the observed outside-in galaxy chemical enrichment (Harris & Zaritsky 2009; Carrera et al. 2011; Meschin et al. 2014). Star clusters share the metallicities of their birthplaces. Nevertheless, with time they drift away from their birth locations. Interactions and other perturbations may produce additional velocity components. Indeed, the derived cluster metallicity value (<[Fe/H]> = -0.45 ± 0.15 dex) is typical of the stellar population located within ~ 2 degrees from the LMC centre, whereas the one expected for the new star cluster deprojected distance ($\rho = 4.63 \pm 0.03^\circ$) is in the outer disc [Fe/H] range. This appears also to be the case, for instance, of other clusters younger than 2–3 Gyr with metallicities similar to that of the inner disc that are observed in the outer disc (Grocholski et al. 2006; Piatti & Geisler 2013). Thirdly, the stellar density map of the new star cluster looks clearly elongated along the SW–NE direction (see Fig. 5), which may be a sign of tidal effects. Indeed, the position of the star cluster in the r_c/r_h versus r_h/rt plane suggests an object that has expanded up to its tidal radius (Heggie & Hut 2003, see e.g. their figure 33.2), while its size is comparable to the LMC globular clusters formed/steadily orbiting at deprojected distances $\lesssim 1$ degree; globular clusters at $\rho \sim 5$ degrees are on average 2–3 times bigger in radius (Piatti & Mackey 2018). This means that the star cluster has the typical size of the innermost ones, but lies in the outer LMC disc. All of these arguments suggest that this cluster was born much closer to the centre of the LMC and somehow was scattered to its current location.

5 CONCLUSIONS

We have carried out a photometric and spectroscopic study using SOAR and Gemini observatory facilities of a recently new discovered LMC star cluster, whose first-derived astrophysical properties suggested that it was an object that was born in the inner LMC disc and soon after ejected outwards into the intergalactic space, reaching a distance similar to that of the SMC.

From accurate RV measurements of upper MS and red giant stars from the CaII infrared triplet spectral region we assigned cluster memberships and estimated the mean star cluster RV and metallicity. Assuming a disc-like geometry, we found that the circular velocity of a disc that rotates with the corresponding star cluster RV at the cluster deprojected distance is nearly 60 per cent higher than that derived for most of the outer LMC disc clusters. The possibility that the new star cluster has reached the outer LMC disc, after being born in the innermost regions of the galaxy is supported by:

- the mean cluster distance (47.9 kpc) derived by fitting theoretical isochrone to the cluster CMD. The latter was built with stars distributed within the cluster radius, while the fit involved only two free parameters, namely: the cluster age and distance modulus, and relied on the positions of RV member stars;
- the mean cluster age (0.9 Gyr), typical of star clusters mainly formed along the LMC bar; the deprojected cluster distance from the LMC centre is $\rho = 4.6$ degrees (3.8 kpc);
- the mean cluster metallicity (<[Fe/H]> = -0.45 ± 0.15 dex) derived from the CaII triplet line equivalent widths technique of red giant members. This metal content is compatible with that from an outside-in formation scenario that brought more enriched gas out of which star clusters were born towards the innermost regions;
- the cluster structural parameters derived from the fits of King (1962), Elson et al. (1987), and Plummer (1911) models to the cluster stellar density radial profile extended from 0.1 out to 250 arcsec from the cluster centre; the cluster radius is 31.6 arcsec (7.3 pc).

ACKNOWLEDGEMENTS

Based on observations obtained at the Gemini Observatory, which is operated by the Association of Universities for Research in Astronomy, Inc., under a cooperative agreement with the NSF on behalf of the Gemini partnership: the National Science Foundation (United States), the National Research Council (Canada), CONICYT (Chile), Ministerio de Ciencia, Tecnología e Innovación Productiva (Argentina), and Ministério da Ciência, Tecnologia e Inovação (Brazil). Based on observations obtained at the Southern Astrophysical Research (SOAR) telescope, which is a joint project of the Ministério da Ciência, Tecnologia, Inovações e Comunicações (MCTIC) do Brasil, the U.S. National Optical Astronomy Observatory (NOAO), the University of North Carolina at Chapel Hill (UNC), and Michigan State University (MSU). We thank the referee for the thorough reading of the manuscript and timely suggestions to improve it.

Downloaded from https://academic.oup.com/mnras/article/482/1/980/5128516 by guest on 01 February 2021

REFERENCES

Belokurov V., Koposov S. E., 2016, MNRAS, 456, 602
Bertin E., Arnouts S., 1996, A&AS, 117, 393
Bica E., Geisler D., Dottori H., Clariá J. J., Piatti A. E., Santos J. F. C., Jr., 1998, AJ, 116, 723
Bica E., Bonatto C., Dutra C. M., Santos J. F. C., 2008, MNRAS, 389, 678
Bica E., Santiago B., Bonatto C., Garcia-Dias R., Kerber L., Dias B., Barbuy B., Balbinot E., 2015, MNRAS, 453, 3190
Bressan A., Marigo P., Girardi L., Salasnich B., Dal Cero C., Rubele S., Nanni A., 2012, MNRAS, 427, 127
Carrera R., Gallart C., Pancino E., Zinn R., 2007, AJ, 134, 1298
Carrera R., Gallart C., Aparicio A., Hardy E., 2011, AJ, 142, 61
Casetti-Dinescu D. I., Moni Bidin C., Girard T. M., Méndez R. A., Vieira K., Korchagin V. I., van Altena W. F., 2014, ApJ, 784, L37
Cenarro A. J., Cardiel N., Gorgas J., Peletier R. F., Vazdekis A., Prada F., 2001, MNRAS, 326, 959
Cole A. A., Smecker-Hane T. A., Tolstoy E., Bosler T. L., Gallagher J. S., 2004, MNRAS, 347, 367
Cole A. A., Tolstoy E., Gallagher J. S., III, Smecker-Hane T. A., 2005, AJ, 129, 1465
Da Costa G. S., 2016, MNRAS, 455, 199
Elson R. A. W., Fall S. M., Freeman K. C., 1987, ApJ, 323, 54
Feitzinger J. V., Weiss G., 1979, A&AS, 37, 575
Fraga L., Kunder A., Tokovinin A., 2013, AJ, 145, 165
Gimeno G. et al., 2016, in Christopher J. E., Luc S., Hideki T., eds, Proc. SPIE Conf. Ser., Vol. 9908, Ground-based and Airborne Instrumentation for Astronomy VI. SPIE, Bellingham, p. 99082S
Glatt K., Grebel E. K., Koch A., 2010, A&A, 517, A50
Grocholski A. J., Cole A. A., Sarajedini A., Geisler D., Smith V. V., 2006, AJ, 132, 1630
Hammer F., Yang Y. B., Flores H., Puech M., Fouquet S., 2015, ApJ, 813, 110
Hanuschik R. W., 2003, A&A, 407, 1157
Harris J., Zaritsky D., 2009, AJ, 138, 1243
Heggie D., Hut P., 2003, The Gravitational Million-Body Problem: A Multi-disciplinary Approach to Star Cluster Dynamics, Cambridge Univ. Press, Cambridge
Hook I. M., Jørgensen I., Allington-Smith J. R., Davies R. L., Metcalfe N., Murowinski R. G., Crampton D., 2004, PASP, 116, 425
Indu G., Subramaniam A., 2015, A&A, 573, A136
Kallivayalil N., van der Marel R. P., Besla G., Anderson J., Alcock C., 2013, ApJ, 764, 161
King I., 1962, AJ, 67, 471
Mackey A. D., Koposov S. E., Erkal D., Belokurov V., Da Costa G. S., Gómez F. A., 2016, MNRAS, 459, 239
McLaughlin D. E., Harris W. E., Hanes D. A., 1994, ApJ, 422, 486
Meschin I., Gallart C., Aparicio A., Hidalgo S. L., Monelli M., Stetson P. B., Carrera R., 2014, MNRAS, 438, 1067
Moni Bidin C., Casetti-Dinescu D. I., Girard T. M., Zhang L., Méndez R. A., Vieira K., Korchagin V. I., van Altena W. F., 2017, MNRAS, 466, 3077
Piatti A. E., 2014, MNRAS, 437, 1646
Piatti A. E., 2016, MNRAS, 459, L61
Piatti A. E., 2017, ApJ, 834, L14
Piatti A. E., Geisler D., 2013, AJ, 145, 17
Piatti A. E., Mackey A. D., 2018, MNRAS, 478, 2164
Piatti A. E., Geisler D., Sarajedini A., Gallart C., 2009, A&A, 501, 585
Piatti A. E., de Grijs R., Rubele S., Cioni M.-R. L., Ripepi V., Kerber L., 2015, MNRAS, 450, 552
Piatti A. E., Hwang N., Cole A. A., Angelo M. S., Emptage B., 2018, MNRAS, 481, 49
Pieres A. et al., 2016, MNRAS, 461, 519
Plummer H. C., 1911, MNRAS, 71, 460
Salem M., Besla G., Bryan G., Putman M., van der Marel R. P., Tonnesen S., 2015, ApJ, 815, 77
Salinas R., Alabi A., Richtler T., Lane R. R., 2015, A&A, 577, A59
Salinas R., Contreras Ramos R., Strader J., Hakala P., Catelan M., Peacock M. B., Simunovic M., 2016, AJ, 152, 55
Schirmer M., 2013, ApJS, 209, 21
Schommer R. A., Suntzeff N. B., Olszewski E. W., Harris H. C., 1992, AJ, 103, 447
Sharma S., Borissova J., Kurtev R., Ivanov V. D., Geisler D., 2010, AJ, 139, 878
Sitek M. et al., 2016, Acta Astron., 66, 255
Stetson P. B., 1987, PASP, 99, 191
Stetson P. B., 1992, J. R. Astron. Soc. Can., 86, 71
Taylor M. B., 2006, in Gabriel C., Arviset C., Ponz D., Enrique S., eds, ASP Conf. Ser. , Vol. 351, Astronomical Data Analysis Software and Systems XV. Astron. Soc. Pac., San Francisco, p. 666
Tokovinin A., Cantarutti R., Tighe R., Schurter P., Martinez M., Thomas S., van der Bliek N., 2016, PASP, 128, 125003
Tonry J., Davis M., 1979, AJ, 84, 1511
van der Marel R. P., Kallivayalil N., 2014, ApJ, 781, 121
van der Marel R. P., Alves D. R., Hardy E., Suntzeff N. B., 2002, AJ, 124, 2639

SUPPORTING INFORMATION

Supplementary data are available at *MNRAS* online.

table 1: photometry of the studied cluster.

Please note: Oxford University Press is not responsible for the content or functionality of any supporting materials supplied by the authors. Any queries (other than missing material) should be directed to the corresponding author for the article.

This paper has been typeset from a TEX/LATEX file prepared by the author.

Downloaded from https://academic.oup.com/mnras/article/482/1/980/5128516 by guest on 01 February 2021